PHOTONICS Research

Integrated photonic RF self-interference cancellation on a silicon platform for full-duplex communication

Xiuyou Han,†,* Xinxin Su,† Meng Chao, Xindi Yang, Weiheng Wang, Shuangling Fu, Yicheng Du, Zhenlin Wu, and Mingshan Zhao

School of Optoelectronic Engineering and Instrumentation Science, Dalian University of Technology, Dalian 116024, China
†*These authors contributed equally to this work.*
**Corresponding author: xyhan@dlut.edu.cn*

Received 20 January 2023; revised 21 July 2023; accepted 24 July 2023; posted 28 July 2023 (Doc. ID 485157); published 21 September 2023

In-band full-duplex (IBFD) technology can double the spectrum utilization efficiency for wireless communications, and increase the data transmission rate of B5G and 6G networks and satellite communications. RF self-interference is the major challenge for the application of IBFD technology, which must be resolved. Compared with the conventional electronic method, the photonic self-interference cancellation (PSIC) technique has the advantages of wide bandwidth, high amplitude and time delay tuning precision, and immunity to electromagnetic interference. Integrating the PSIC system on chip can effectively reduce the size, weight, and power consumption and meet the application requirement, especially for mobile terminals and small satellite payloads. In this paper, the silicon integrated PSIC chip is presented first and demonstrated for IBFD communication. The integrated PSIC chip comprises function units including phase modulation, time delay and amplitude tuning, sideband filtering, and photodetection, which complete the matching conditions for RF self-interference cancellation. Over the wide frequency range of C, X, Ku, and K bands, from 5 GHz to 25 GHz, a cancellation depth of more than 20 dB is achieved with the narrowest bandwidth of 140 MHz. A maximum bandwidth of 630 MHz is obtained at a center frequency of 10 GHz. The full-duplex communication experiment at Ku-band by using the PSIC chip is carried out. Cancellation depths of 24.9 dB and 26.6 dB are measured for a bandwidth of 100 MHz at central frequencies of 12.4 GHz and 14.2 GHz, respectively, and the signal of interest (SOI) with 16-quadrature amplitude modulation is recovered successfully. The factors affecting the cancellation depth and maximum interference to the SOI ratio are investigated in detail. The performances of the integrated PSIC system including link gain, noise figure, receiving sensitivity, and spurious free dynamic range are characterized.

https://doi.org/10.1364/PRJ.485157

1. INTRODUCTION

Nowadays, the rare spectrum resource has become one of the major factors limiting the development of wireless communication, not only for B5G and 6G networks, but also for the new generation satellite communications [1]. In-band full-duplex (IBFD) technology can realize simultaneously transmitting and receiving radio frequency (RF) signals at the same frequency band, which significantly increases spectrum efficiency and doubles the data transmission rate [2–4]. However, during IBFD communication, the high-power signal sent from the transmitting antenna will interfere with the low-power signal of interest (SOI), which is also received by the receiving antenna. It is called RF self-interference, and cannot be filtered out by a notch filter due to the spectrum overlap between the SOI and the interference. Therefore, RF self-interference cancellation (SIC) is essential for the application of IBFD technology.

RF SIC technology includes spatial cancellation, analog domain cancellation, and digital domain cancellation [5–8]. Among them, the analog domain cancellation is a very important stage to suppress RF self-interference to enough low-power levels to ensure that the analog to digital conversion (ADC) unit avoids being saturated and works within the dynamic range. The electronic methods for analog domain RF SIC are generally limited by the bandwidth as well as the amplitude and phase tuning precision of RF devices, and it is difficult to obtain high cancellation depth over a wide RF band.

Compared with electronic methods, photonic SIC (PSIC) has the advantages of wide bandwidth, high amplitude and delay tuning precision, and immunity to electromagnetic interference. In recent years, many kinds of PSIC schemes have been proposed with demonstration of the above advantages [9]. The dual Mach–Zehnder modulator (MZM)-based PSIC system

was first reported to suppress RF self-interference, which was biased at the orthogonal points of the positive slope and negative slope [10]. Since then, PSIC schemes have been presented successively by using a dual-drive MZM (DD-MZM) [11], dual-parallel MZM (DP-MZM) [12], and DP polarization modulator (DP-PolM) [13], where the phase inversion between the interference path and reference path was completed by direct current (DC) bias control. Phase inversion can also be realized in the optical domain by phase modulation and sideband filtering [14] and cross-gain modulation of a semiconductor optical amplifier [15], or in the electronic domain by using Balun [16] and a balanced photodetector (PD) [17,18]. For a realistic scenario, multipath PSIC schemes should be considered to eliminate interference signals caused by reflection, scattering, and diffraction. Multipath PSIC systems were constructed through a single-mode to multimode (SM-MM) combiner [19,20], dispersive element [21], phase modulation and wavelength division multiplexing [22], and fiber Bragg grating (FBG)-based delay line [23,24]. Recently, RF signals over fiber transmission [25], frequency downconversion [26,27], and image-reject mixing [28] were also studied when achieving RF SIC at the same time. The above-mentioned schemes have made impressive contributions to the progress of IBFD communication. However, they are all based on discrete optoelectronic devices, which may suffer from bulky volume and high power consumption, and cannot satisfy the miniaturization requirement of mobile terminals, unmanned aerial vehicles (UAV), and small satellite payloads.

The rapid development of photonic integration technology gives impetus to the advance of microwave photonics (MWP) technology [29,30]. Through integration of discrete optoelectronic devices on chip, the size, weight, and power consumption (SWaP) of the MWP system and the coupling loss between devices can be tremendously reduced, and system stability can be improved greatly [31]. The integrated PSIC chip was first proposed and characterized on an indium phosphide (InP) platform [32,33]. It utilized a pair of DC-driven semiconductor optical amplifiers to realize the adjustment of amplitude and phase of the reference signal, with the RF SIC demonstration in Long Term Evolution (LTE) and WiFi bands. Continuous work was implemented to improve the link gain and noise figure by the external modulation and balanced detection [34]. The silicon photonic integrated chip has the benefits of the ability for high laser powers and lower process variation yield, and has been attracting much attention for PSIC in recent years. The silicon photonic integrated MWP filter for amplitude tuning with off-chip delays was primarily investigated for RF SIC [35]. The DP-MZM was designed and fabricated on IMEC's silicon-on-insulator iSiPP50G platform for the application of RF SIC [36], with the tuning of amplitude and delay time by RF devices. However, the instantaneous bandwidths and operation RF band of the reported integrated PSIC systems are relatively narrow.

In this paper, the first silicon integrated PSIC chip is presented and demonstrated experimentally. Here, the phase modulator (PM), variable optical attenuator (VOA), tunable optical delay line (TODL), wavelength division multiplexer (WDM), optical filter (OF), and PD are fully integrated on one chip to construct an MWP subsystem with the function of regulating the amplitude and time delay of optically carried RF signals to cancel the RF self-interference over a broad band. The scheme has the advantages of a specific out-of-phase property between the right and left sidebands of optically filtered phase modulation signals, and no need for complicated DC bias control as with intensity modulation [10–13]. Through a comprehensive investigation including the function unit and subsystem design, PSIC chip characterization, and optical, electrical, and RF co-package, the integrated PSIC module operates over the broad range of C, X, Ku, and K bands. The IBFD in Ku band of satellite communication is demonstrated with the successful recovery of the SOI. The factors affecting the cancellation depth and maximum interference to SOI ratio of the integrated PSIC system are measured and analyzed in detail. In addition, the performances of the integrated PSIC system including the link gain, noise figure, receiving sensitivity, and spurious free dynamic range (SFDR) are characterized.

2. PSIC SYSTEM ARCHITECTURE AND CHIP DESIGN

The structure of the integrated PSIC system on a silicon photonic platform is shown in Fig. 1. The operation principle of the proposed PSIC system is based on phase modulation and optical sideband filtering to realize the phase conversion between reference and interference signals. The received signals, including the SOI $s(t)$ and interference signal $i(t)$, are phase modulated on the optical carrier λ_1 via PM_1, which is called the interference branch. The reference signal $r(t)$ tapped from the transmitter (Tx) is phase modulated on the optical carrier λ_2 via PM_2, which is called the reference branch. The reference signal passes through the VOA and TODL to experience the adjustment of amplitude and time delay.

The VOA is composed of a Mach–Zehnder interferometer (MZI) structure with a phase shifter on one arm to implement the output intensity tuning. This MZI is a symmetric structure with equal interference arms of 120 μm. The TODL is formed by cascading two ring resonators with the same perimeter of 125 μm and one phase shifter on each ring waveguide. The ring resonators operate in the anti-resonant state to obtain the time delay with low loss [37]. The delay amount is regulated by adjusting the additional phase on the two rings. The phase modulated interference and reference signals are combined via the WDM and input to the OF. The structure of WDM is an MZI with unequal length arms, which has much lower coupling loss and higher scalability compared with the direction coupler. The arm length difference is 570.5 μm, corresponding to a free spectral range (FSR) of 1 nm. The phase shifter is also designed on one arm to achieve flexible regulation of the multiplexing wavelength. To realize a broad frequency band for SIC, the OF should have a "box-like" filtering response shape to filter out one sideband at low frequency and simultaneously retain the other sideband at high frequency. Here, the ring assisted MZI structure is utilized to implement the function [38]. To regulate the filtering response shape conveniently, the couplers in the OF are MZI structures with adjustable coupling coefficients [39]. The phase shifters are also set on the ring waveguide and the long arm waveguide to realize

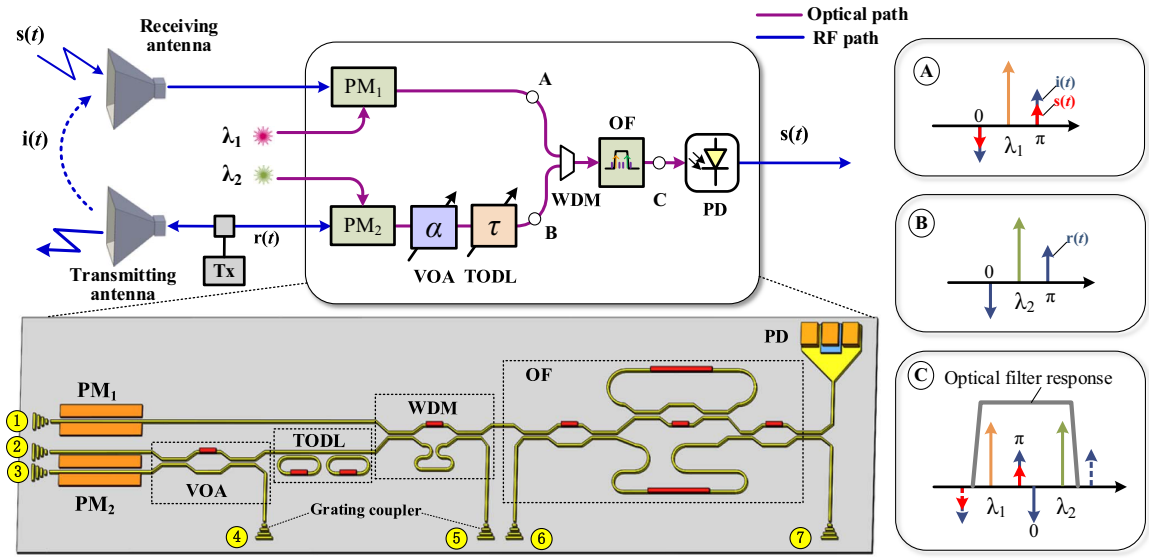

Fig. 1. Structure of the integrated PSIC system and schematic spectra illustrating phase modulation and sideband filtering. PM, phase modulator; VOA, variable optical attenuator; TODL, tunable optical delay line; WDM, wavelength division multiplexer; OF, optical filter; PD, photodetector.

phase tuning to optimize the filtering response. The sideband filtering of phase modulation signals is completed by the OF as the schematic spectra at point C shows in Fig. 1. The +1st-order sideband of the interference branch and the −1st-order sideband of the reference branch are retained within the OF passband. The two single-sideband with carrier (SSB-C) signals are input to the PD, upon which two anti-phase RF components are detected and cancel each other. As a result, the interference signal is eliminated and the SOI is recovered.

Silicon photonics leverages the maturity and know-how of silicon complementary metal–oxide semiconductor (CMOS) processing techniques and is a suitable platform for large-scale photonic integrated circuits [40]. The integrated PSIC system was fabricated on a standard 220 nm silicon-on-insulator platform. Figure 2(a) shows the optical microscope image of the PSIC chip with an area of 1.1 mm × 5 mm, where the structures of PMs (PM_1 and PM_2), VOA, TODL, WDM, OF, and PD are marked. Figure 2(b) shows a cross-sectional schematic view of the silicon-on-insulator platform. Here, to meet the single-mode transmission of 1550 nm wavelength, the width of the passive strip waveguide is designed at 450 nm. The modulation arm length of PM_1 and PM_2 is 3 mm, and

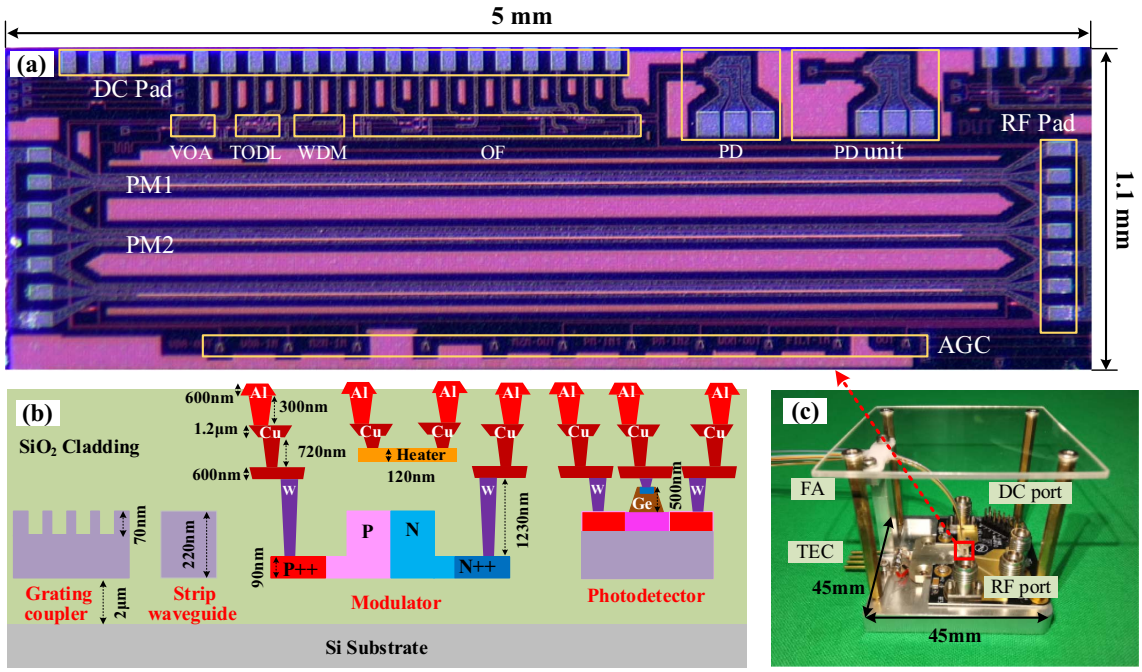

Fig. 2. (a) Optical microscope image of the integrated PSIC chip. (b) Cross-sectional schematic view (not to scale) of the silicon-on-insulator platform. (c) Packaged PSIC module. AGC, array grating coupler; TEC, thermo-electric cooler; FA, fiber array.

provided with N-type and P-type implantations for PN junctions in rib waveguides. To regulate the VOA, TODL, WDM, and OF, TiN heaters are deposited on top of the strip waveguides as phase shifters. The waveguide grating couplers marked as ①–⑦ in Fig. 1 are arranged in an array with a pitch of 250 μm on the integrated PSIC chip, which is helpful to package with a fiber array. The packaged PSIC module is shown in Fig. 2(c). The RF and DC paths on the printed circuit board (PCB) were designed for transmitting RF signals, regulating phase shifters, and driving PD in the chip. To achieve a broad operation band, the length of gold wire to the modulators and PD should be as short as possible, about 0.5–0.7 mm, and 50 Ω impedance matching modulators were also provided. Wires were made on the DC pads with a length of about 1 mm. The waveguide grating couplers were coupled with a polarization-maintaining fiber array at a polished end angle of 8° and fixed with ultraviolet glue. The coupling loss between the packaged waveguide grating and fiber is about 4 dB per port. The wire-bonded chip on the PCB is fixed on a metal base, and the thermo-electric cooler (TEC) is installed under the chip to make it work stably.

3. EXPERIMENTAL RESULTS

A. Test of Function Units in the PSIC Chip

Before the RF SIC measurement, the function units in the PSIC chip including the VOA, TODL, WDM, OF, and PD were characterized first.

1. VOA

The VOA acts as the amplitude tuning unit for the phase modulated RF signal in the optical domain. The phase shifter on one of the arms of MZI is based on the thermo-optic effect. The TiN heater with a thickness of 120 nm and length of 100 μm was measured with a resistance of 580 Ω. The second and fourth waveguide grating couplers, namely, ② and ④ in Fig. 1, are utilized as the input and output optical ports for measurement, respectively. The cross optical output was monitored with an optical power meter (EXFO, FPM-602) when the DC voltage from the multi-channel power (NI, PXIe-4163) was applied on the heater. The relationship between the output optical power and applied DC power is plotted in Fig. 3(a) exhibiting a cosine curve. According to the operation principle of MZI-based VOA, the required DC power to obtain a phase shift of π is about 44.8 mW. The 0.2 mV adjustment accuracy of the DC power supply makes the output optical power adjustable continuously.

Subsequently, the amplitude tuning response over a certain wavelength range was measured by the optical vector analyzer (OVA, LUNA 5000), and the results are shown in Fig. 3(b). The standard resolution of scanning wavelength is 1.6 pm. The amplitude response is flat over 2.54 nm, about 317.5 GHz, which ensures equal amplitude tuning for a broad band. A maximum amplitude tuning range of 33 dB is realized with the power of about 44.8 mW, which corresponds to a thermal regulated phase difference of π between the two arms of MZI structure. The power consumption is relatively high, which is mainly due to the thermal cross talk between the two adjacent arms. The air grooves can be etched beside the heater to reduce thermal cross talk, which can be realized by the waveguide

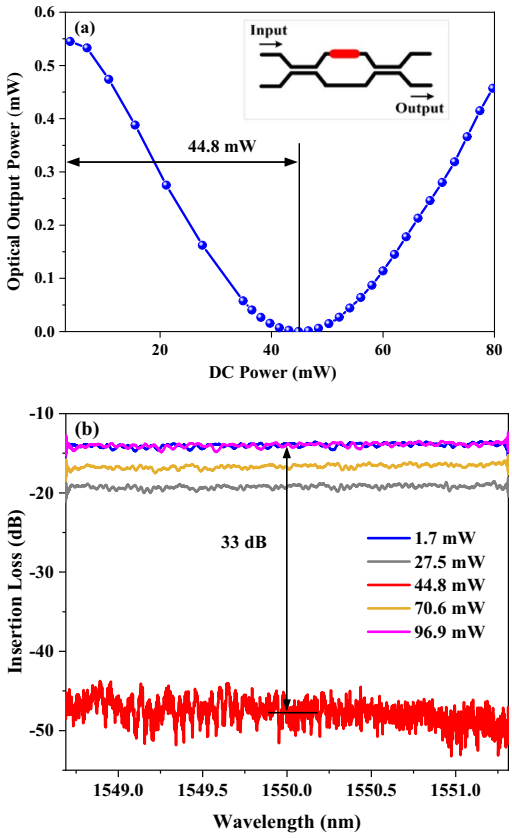

Fig. 3. Measured results of VOA. (a) Variation curve of output optical power with applied DC power. (b) Measured optical spectrum of different applied powers over 2.54 nm bandwidth.

manufacturing craft [41]. It is simulated that power consumption is about 20 mW to obtain π phase difference for the MZI structure with air grooves.

2. TODL

The delay response of the TODL unit on chips was characterized by the OVA. With a single scanning, the OVA can simultaneously measure the complete transfer response of photonic devices including insertion loss and group delay versus wavelength. Figure 4(a) shows the relative intensity response of the two cascaded rings with different driving DC powers (Pr1 and Pr2) on the two heaters. The resonant wavelengths of the two rings align with each other when DC powers are 10.3 mW and 11.4 mW. The measured FSR of the ring is 4.5 nm, which is consistent with the designed ring perimeter. Figures 4(b) and 4(c) show the zoom-in intensity response around 1550 nm and the corresponding time delay response. As can be seen clearly, in case 1, $\mathrm{Pr}1 = 10.3$ mW and $\mathrm{Pr}2 = 11.4$ mW, the two rings operate in the resonant state around 1550 nm. In case 2, $\mathrm{Pr}1 = 14.3$ mW and $\mathrm{Pr}2 = 7.4$ mW, different phase shifts are applied to the two rings, namely, one is $+\Delta\varphi$, and the other is $-\Delta\varphi$. $\Delta\varphi$ has a linear relationship with the DC power applied to the heater. The resonant wavelengths of the two rings separate from each other, and the intensity response trends to be flat. In case 3, $\mathrm{Pr}1 = 18.9$ mW and $\mathrm{Pr}2 = 2.8$ mW, the two rings operate

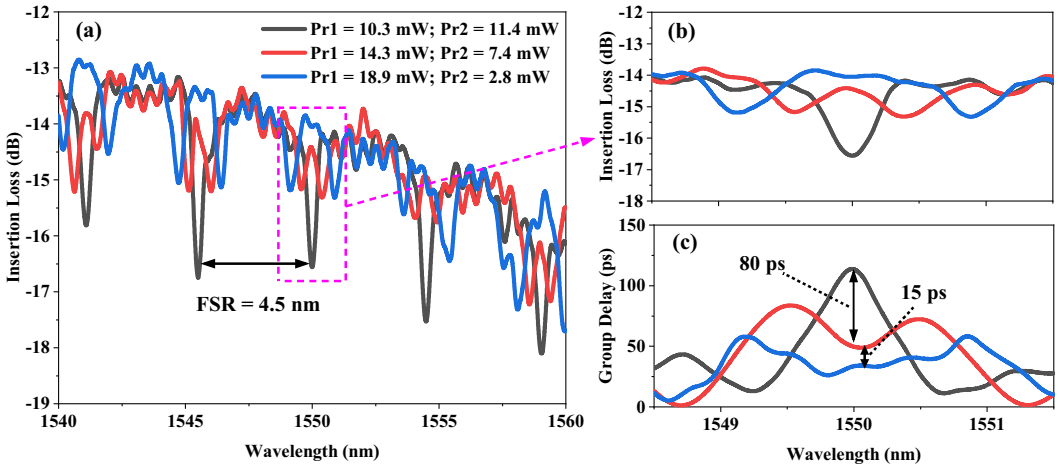

Fig. 4. Measured optical spectrum of TODL. (a) Intensity response under different regulation states. (b) Zoom-in view of (a) around 1550 nm. (c) Group delay response corresponding to different regulation states in (b).

in the anti-resonant state and the intensity loss is minimum. It can be seen from Figs. 4(b) and 4(c) that the relative time delay adjustment from 15 ps to 80 ps is realized with intensity fluctuation of about 2.5 dB, which can be compensated for by the VOA in the reference branch.

3. WDM

The MZI-based WDM is designed as a combiner for two different optical wavelengths. Figure 5(a) shows the simulation results, where the red curve is the intensity response from input port I1 to output port O1, and the blue curve is from input port I2 to output port O1. To ensure low transmission loss, wavelengths of λ_1 and λ_2 correspond to the positions of the maximum response values in respective periods. Here, intervals of λ_1 and λ_2 are designed as 0.5 nm, which is a half FSR of the MZI structure. Then, the intensity response of WDM was measured by the OVA. A light wave enters the first waveguide grating coupler ① and exits from the fifth one ⑤, as marked in Fig. 1. Applying DC voltage to the heater of the upper arm waveguide can realize wavelength adjustment, thus improving the flexibility of wavelength selection in the experiment. Figure 5(b) shows the measured results. The resistance of the heater is 600 Ω. The blue curve is the intensity response with zero voltage; the FSR is about 1 nm, which is consistent with the blue curve in Fig. 5(a). The transmission spectra of the WDM were measured according to different applied powers on the heater at about 26.7 mW (yellow curve), 48.5 mW (gray curve), and 66.8 mW (red curve). With the power of 66.8 mW, the wavelength tunable range of 0.5 nm, namely, a half FSR of the MZI structure, is achieved.

4. OF

The OF implements the function of sideband filtering to realize conversion from phase modulation to intensity modulation and the phase inversion between interference and reference branches. To obtain the box-like filtering response of the ring assisted MZI structure, five phase shifters in the OF as shown in Fig. 1 are designed to tune the coupling coefficients and the additional phase on the ring waveguide and the long arm waveguide. The filtering response can be characterized easily because the PSIC chip has been packaged with fiber array and DC ports. The sixth and seventh waveguide grating couplers, namely, ⑥ and ⑦ in Fig. 1, are utilized as the input and output optical ports for measurement, respectively, which can represent the filtering response from the WDM to the PD due to the symmetric property of the ring assisted MZI

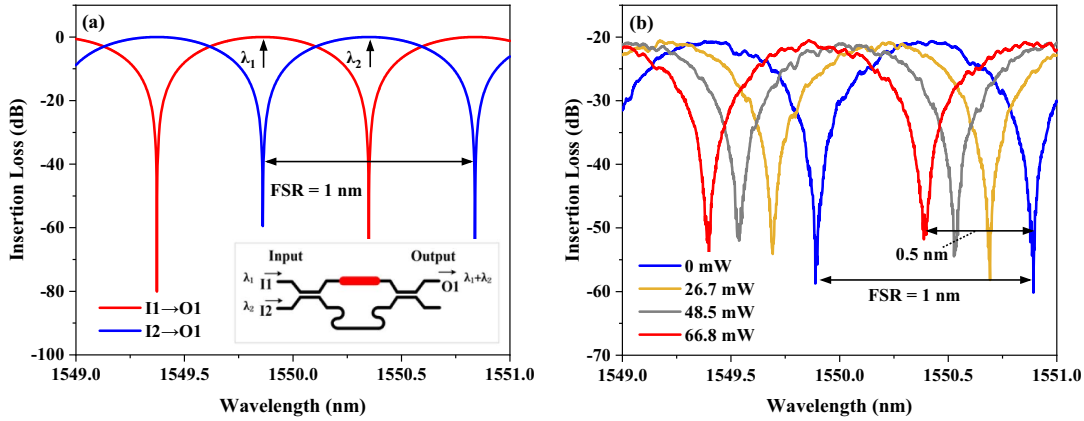

Fig. 5. Transmission spectra of the WDM. (a) Simulated result. (b) Measured intensity response with different applied powers.

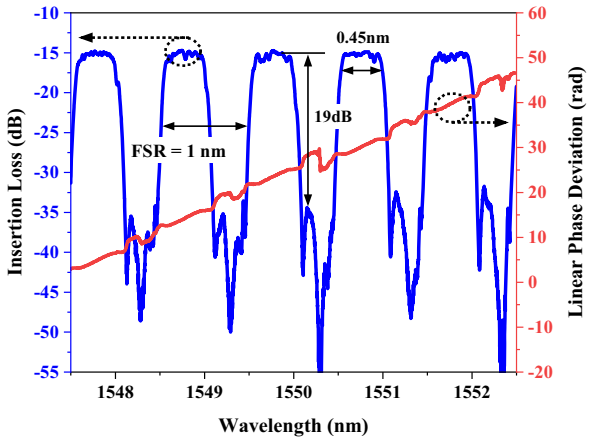

Fig. 6. Measured intensity and phase response of the OF.

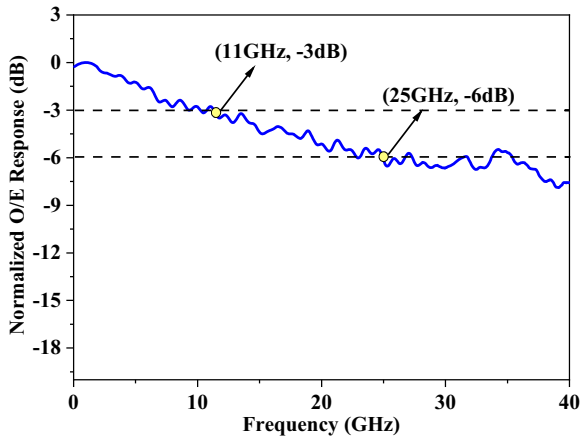

Fig. 7. Measured O/E conversion response of the PD.

structure. Figure 6 shows the measured intensity (blue) and phase (red) response curves of the OF. The out-of-band rejection ratio is 19 dB, the 3 dB bandwidth is 0.45 nm, and the FSR is 1 nm. According to the 3 dB bandwidth and sideband filtering principle, the maximum frequency band of about 56 GHz can be operated. It can be seen from Fig. 6 that the phase response within the passband is linear, and it indicates that the time delay is equal in the operation frequency band.

5. PD

PD is used for the optical-electrical (O/E) conversion. As marked in Fig. 2, the characterized PD unit is composed of a waveguide grating coupler and a germanium PD. We tested the PD unit using a vector network analyzer (VNA, Keysight N5247B) and a commercial high-bandwidth intensity modulator (MZM, EO-Space 40 GHz). The RF signal from VNA is modulated on the optical carrier of 1550 nm via the intensity modulator. Here, the MZM operates at the orthogonal point by using a bias point controller. The optically carried RF signal is directly coupled into the on-chip PD through the waveguide grating coupler. The RF probe (GSG, 40 GHz) detects the output RF signal from the PD biased with reverse DC voltage. A bias-tee is used to connect the RF probe and the cable to the input port of the VNA, by which reverse DC voltage can be applied to the PD via the probe, and the RF signal can transmit to the VNA. The measured O/E conversion response of the PD is shown in Fig. 7 with reverse DC voltage of −1.5 V, where the frequency responses of the RF cable, bias-tee, and intensity modulator have been removed. It can be seen from Fig. 7 that the 3 dB bandwidth is 11 GHz, and the 6 dB bandwidth is 25 GHz.

B. RF SIC and IBFD Communication Characterization

The experiment setup as shown in Fig. 8 was established to investigate the feasibility of the PSIC module for IBFD communication. λ_1 and λ_2 from two laser sources (NKT-Koheras ADJUSTIK E15, Emcore1782A) are input to the PSIC chip through waveguide grating couplers ① and ③, respectively. The signal from the generator (SG1, Keysight E8267D) is divided into two paths. One is utilized as the interference signal i(t), and the other is the reference signal r(t). The SOI s(t) is output from the other signal generator (SG2, Agilent E8267D). The SOI and the interference signal are combined and modulated on the optical carrier of 1549.65 nm (λ_1) in the interference path via PM_1, and the reference signal is modulated on the optical carrier of 1549.15 nm (λ_2) via PM_2. After passing through the TODL and VOA, the optically carried reference signal is combined with the optically carried interference signal via the WDM and input to the OF. The output spectrum from the OF is measured by the optical spectrum analyzer (OSA, AQ6370D), and the SSB-C signals are obtained as the measured optical spectrum shown in Fig. 9. It can be seen from Fig. 9 that the left sideband of the reference branch and the right sideband of the interference branch are filtered out successfully. Then, the filtered signals are input to the on-chip PD. It is found that due to the large coupling loss of grating couplers and transmission loss of on-chip waveguides, the optical power into PD is lower than −13 dBm, which is too poor to recover high-quality microwave signals. Therefore, the optical signal from the other port of OF via the grating coupler ⑦ is amplified by an erbium doped fiber amplifier (EDFA, CEFA-C-HG-PM-50-B130) with output power of 9 dBm and input to the PD (Finisar XPDV2120R-50 GHz) for the following measurement.

1. Operation Bandwidth and Cancellation Depth of PSIC System

The operation bandwidth and cancellation depth of the PSIC system were measured with the scheme shown in the blue dotted line in Fig. 8. The VNA (Keysight N5247B) was used to measure the S_{21} amplitude response of the interference branch and the reference branch [intermediate frequency (IF) bandwidth = 15 kHz]. The results are shown in Fig. 10, showing that the amplitude responses of the two branches are matched well to each other.

The operation frequencies covering C, X, Ku, and K bands are selected to characterize the cancellation performance at 5 GHz, 8 GHz, 10 GHz, 12.4 GHz, 14.2 GHz, 16 GHz, 18 GHz, 20 GHz, and 25 GHz. Over 1 GHz bandwidth at each central frequency, the VOA and TODL in the reference path are adjusted to make the reference signal and interference signal equal in amplitude and opposite in phase, and then the cancellation depth is characterized. The measured results are

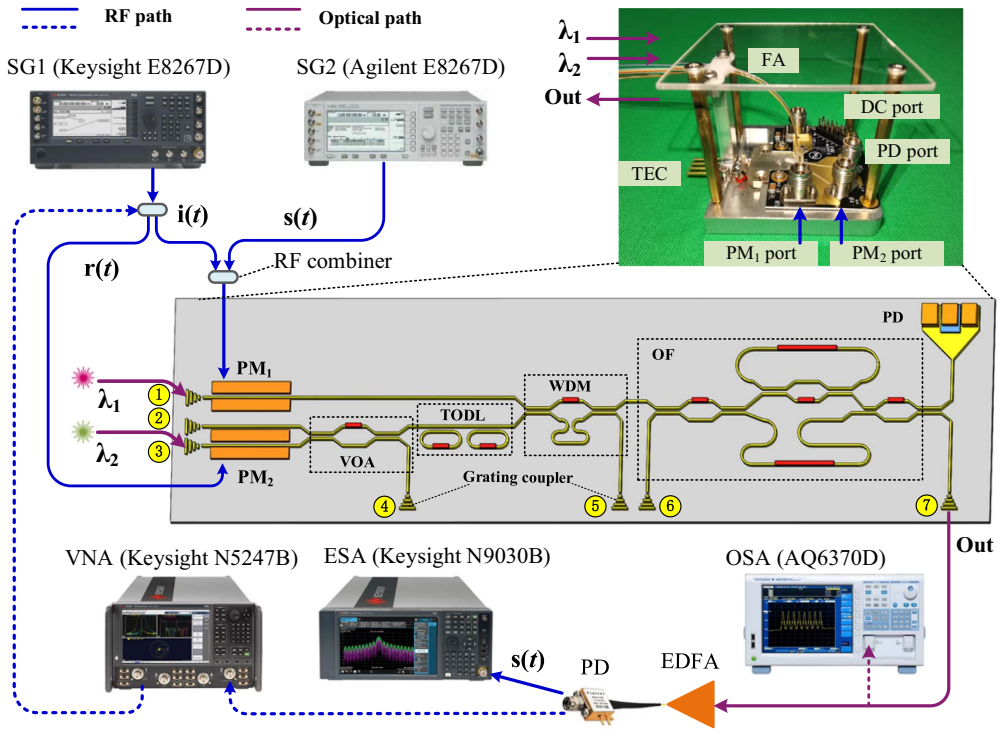

Fig. 8. Experiment setup to demonstrate the feasibility of the PSIC module for IBFD communication.

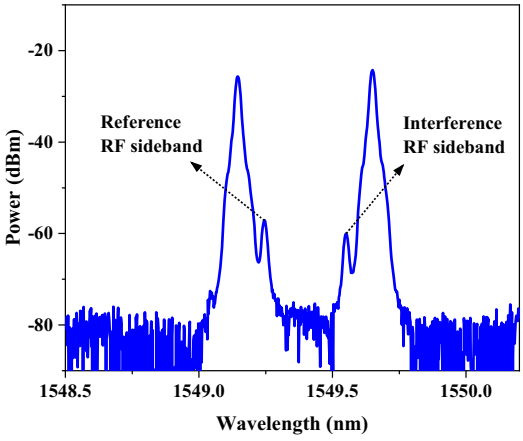

Fig. 9. Optical spectrum of phase-modulated signals by sideband filtering.

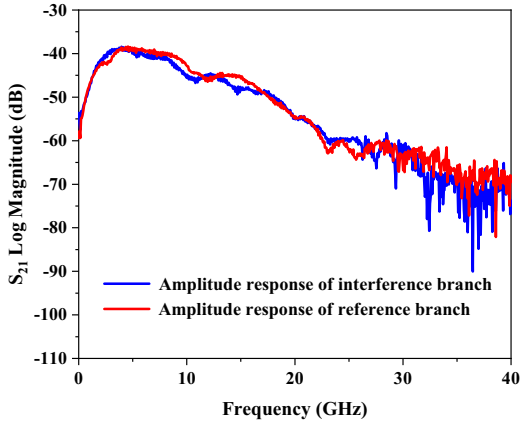

Fig. 10. S_{21} amplitude response of interference branch and reference branch.

shown as the blue curve in Fig. 11. The red line marks the position of the 20 dB cancellation depth, and the orange area is the operation bandwidth for the cancellation depth over 20 dB. It can be seen from Fig. 11 that a cancellation depth of more than 20 dB is achieved with the narrowest bandwidth of 140 MHz for all the selected operation frequencies. A maximum bandwidth of 630 MHz is obtained at a center frequency of 10 GHz.

The cancellation depth that can be achieved within a certain bandwidth is determined by the amplitude deviation and phase deviation between interference and reference branches. Central frequencies of 12.4 GHz and 14.2 GHz in Ku band satellite communication were selected for further analysis of the factors affecting cancellation performance. Figures 12(a) and 12(b) show the amplitude deviation (blue curve) and phase deviation (red curve) between interference and reference branches measured by VNA over 1 GHz bandwidth at central frequencies of 12.4 GHz and 14.2 GHz, respectively. The orange areas in Figs. 12(a) and 12(b) mark the bandwidth with the cancellation depth over 20 dB, indicating that the maximum phase deviation is 5.7°, and the maximum amplitude deviation is 0.82 dB. These are consistent with the theorical analysis [9].

2. Recovery of SOI

An experimental verification for the full-duplex satellite communication of Ku band by using the integrated PSIC module

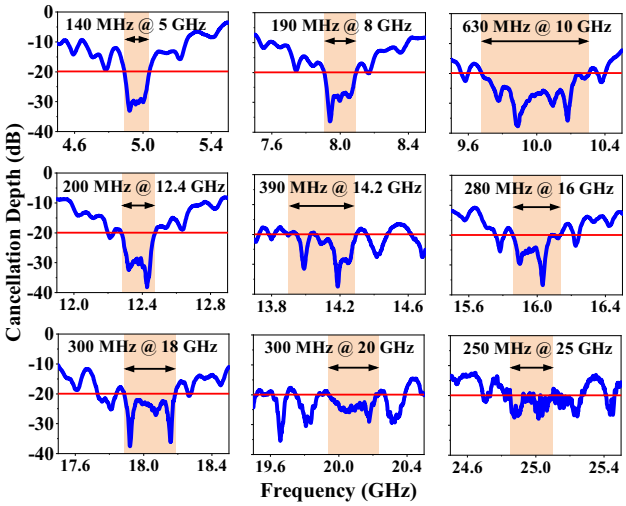

Fig. 11. Cancellation depth characterization in C, X, Ku, and K bands.

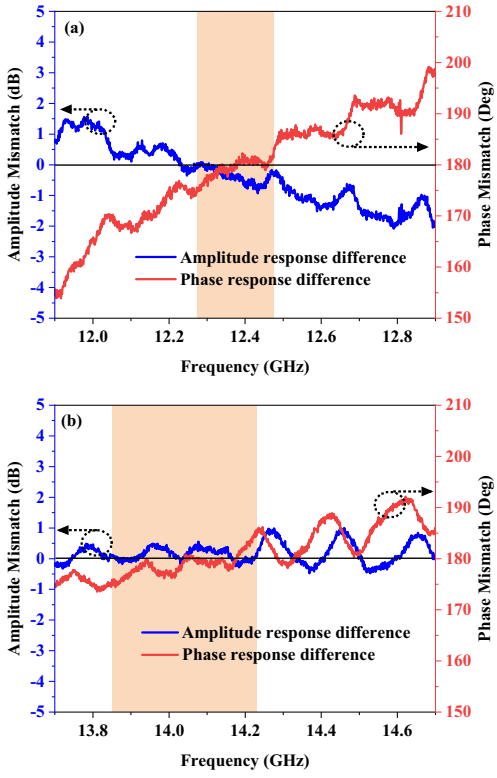

Fig. 12. Measured amplitude and phase differences between reference and interference branches. (a) $f_{RF} = 12.4$ GHz; (b) $f_{RF} = 14.2$ GHz.

was carried out. Additive white Gaussian noise (AWGN) from SG1 with a bandwidth of 100 MHz and power of 18 dBm was utilized as the interference signal. The 16-quadrature amplitude modulation (16QAM) signal with a bandwidth of 50 Msps from SG2 was used as the SOI. After transmitting through the PSIC system, the output signals were measured by an

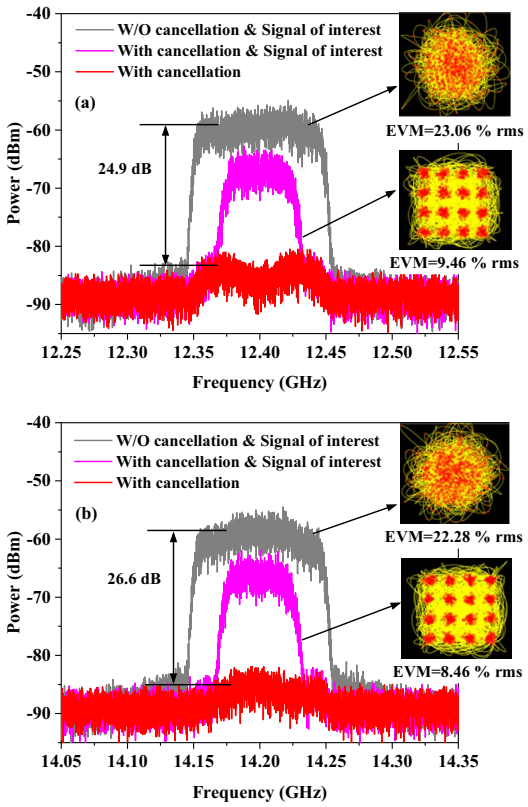

Fig. 13. Output RF spectra in bandwidth of 100 MHz with and without cancellation and constellation diagram of SOI in bandwidth of 50 Msps. (a) $f_{RF} = 12.4$ GHz; (b) $f_{RF} = 14.2$ GHz.

electric spectrum analyzer (ESA, Keysight N9030B). Figures 13(a) and 13(b) show the measured spectra with and without cancellation and the corresponding constellation diagram of recovered SOI. As shown in Fig. 13(a), for a central frequency of 12.4 GHz, the gray curve shows the spectrum without interference cancellation; the SOI is buried by the strong interference signal, and the constellation diagram is cluttered with an error vector magnitude (EVM) of 23.06% rms. After the interference is suppressed, the SOI is recovered as shown in the pink curve with an EVM of 9.46% rms. According to the international 3GPP standard [42], the maximum EVM allowed by 16QAM signal is 12.5% rms. Therefore, the SOI is recovered successfully by the integrated PSIC module. When SG2 is turned off, the red curve shows the spectrum of a residual interference signal, exhibiting a cancellation depth of 24.9 dB. Similarly, as shown in Fig. 13(b), for a center frequency of 14.2 GHz, a cancellation depth of 26.6 dB is achieved with a bandwidth of 100 MHz, and the EVM of the recovered SOI is 8.46% rms.

3. Maximum Interference to SOI Ratio

To characterize the SOI recovery capability of the PSIC system, the maximum interference to SOI ratio η for a certain EVM value of the recovered SOI is defined as

$$\eta = \frac{P_{SI}}{P_{SOI}}, \tag{1}$$

where P_{SI} is the power of the interference signal, and P_{SOI} is the power of SOI. η represents the capability of the PSIC system to eliminate interference and to recover SOI. The higher the value of η, the better the performance of the PSIC-based full-duplex communication system.

First, the central frequency was set at 12.4 GHz, and power and bandwidth of SOI were −4.7 dBm and 50 Msps, respectively. The bandwidth of interference signal was 100 MHz, which is consistent with Fig. 13(a). After achieving SIC, the interference signal power was increased gradually, and the corresponding EVM values of the recovered SOI were measured, with the results shown in Fig. 14(a). With the increase of interference signal power, EVM performance degrades. It can be inferred that the maximum interference signal power of the established system is 5.9 dBm for the 3GPP standard of a 16QAM signal with EVM of 12.5% rms, and the corresponding maximum interference to SOI ratio is 10.6 dB. Similarly, for the other central frequency of 14.2 GHz, as the measured results show in Fig. 14(b), the input power of 16QAM SOI is −6 dBm, and the maximum interference signal power is 4.7 dBm for the required EVM of 12.5% rms, resulting in a maximum interference to SOI ratio of 10.7 dB.

C. MWP System Performance Characterization

1. Gain and Noise Figure

The gain (G) and noise figure (NF) directly affect the performance of the MWP system. The noise figure can be expressed as [43]

$$\mathrm{NF} = 174 - G + P_{\mathrm{noise}}, \tag{2}$$

where P_{noise} is the noise floor of the system. For the PSIC system, the target is to recover the SOI from the interference signal. The gain of the PSIC system can be obtained for the S_{21} response as shown in Fig. 10 with values of −44.7 dB and −47.4 dB at 12.4 GHz and 14.2 GHz, respectively. The measured noise floor P_{noise} by ESA is −144 dBm/Hz. Consequently, the NFs of the PSIC system at 12.4 GHz and 14.2 GHz are 74.7 dB and 77.4 dB, respectively.

2. Receiving Sensitivity

Receiving sensitivity, namely, the minimum signal power that the system can receive for a certain EVM requirement, is utilized to characterize the performance of the PSIC system. At a central frequency of 12.4 GHz, the SOI of 16QAM with a bandwidth of 50 Msps was generated from SG2 and then passed through the PSIC system. The SOI power was increased gradually, and the corresponding EVM values were measured, with the results shown in Fig. 15(a). When the EVM reaches 12.5% rms, the receiving sensitivity of the system is −13.8 dBm. Similarly, the receiving performance of the PSIC system at a central frequency of 14.2 GHz was also measured with the SOI of 16QAM and bandwidth of 50 Msps. The results are shown in Fig. 15(b) with the receiving sensitivity of −10.5 dBm.

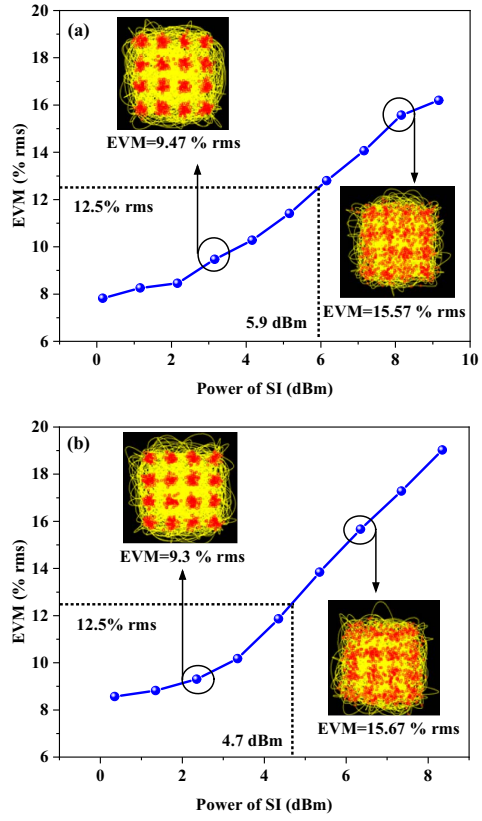

Fig. 14. Measured EVM of the recovered SOI with different powers of interference signal. (a) $f_{\mathrm{RF}} = 12.4$ GHz; (b) $f_{\mathrm{RF}} = 14.2$ GHz.

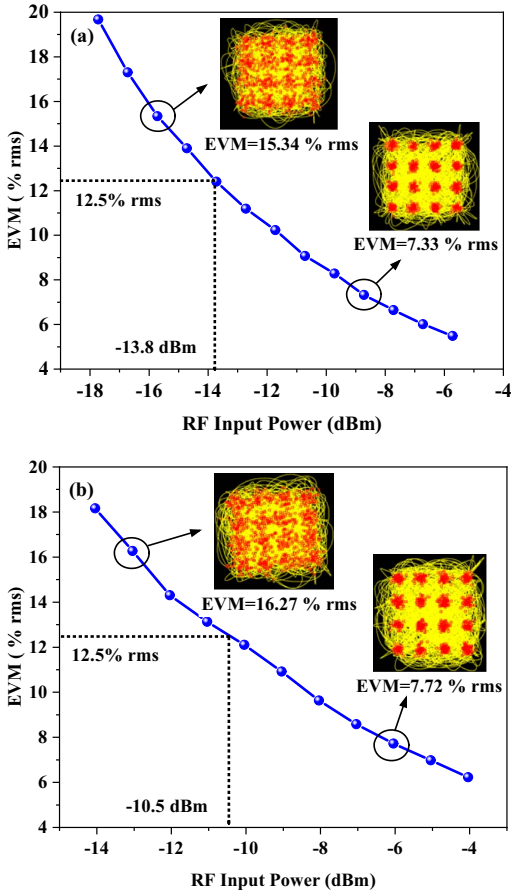

Fig. 15. Measured EVM of SOI after PSIC system with different input powers. (a) $f_{\mathrm{RF}} = 12.4$ GHz; (b) $f_{\mathrm{RF}} = 14.2$ GHz.

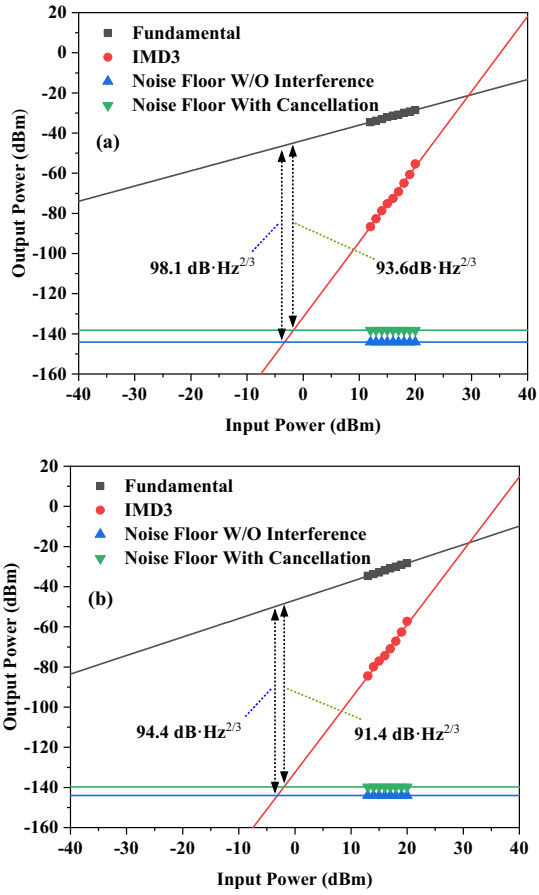

Fig. 16. Measured SFDR of the PSIC system without interference and with cancellation. (a) $f_{RF} = 12.4$ GHz; (b) $f_{RF} = 14.2$ GHz.

3. Spurious Free Dynamic Range

The SFDR is an important parameter of an MWP system influenced by the gain, noise figure, and nonlinear intermodulation. The two-tone test method [43] was applied to measure the SFDR of the established PSIC system. First, the interference signal was not considered with SG1 being turned off. The SFDR of the PSIC system was measured by using a two-tone signal from SG2 with an interval of 10 MHz loaded on PM_1. With the increased power of the two-tone signal, the noise floor of the PSIC system and powers of the fundamental and third-order intermodulation signals were measured by ESA at center frequencies of 12.4 GHz and 14.2 GHz, respectively. The parameters of the ESA were set as RBW = 10 kHz, Span = 50 MHz, Sweep = 515 ms, and Atten = 0 dB, and the results are shown in Fig. 16. It can be seen that the noise floor is the same as −144 dBm/Hz for center frequencies of both 12.4 GHz and 14.2 GHz, as shown in the blue fitting curves in Figs. 16(a) and 16(b), and the corresponding SFDRs are 98.1 dB · $Hz^{2/3}$ and 94.4 dB · $Hz^{2/3}$, respectively.

SG1 is turned on and the interference signal of 18 dBm is input to the integrated PSIC system and then cancelled by the reference signal. The noise floor of the system is affected by the residual interference signal. However, because the interference signal is suppressed much lower than the SOI, the powers of the fundamental and third-order intermodulation signals are consistent with the results when the interference signal is off. The results are also presented in Fig. 16. It can be seen that the noise floors are −138.25 dBm/Hz and −139.75 dBm/Hz for center frequencies of 12.4 GHz and 14.2 GHz, as shown by the green fitting curves in Figs. 16(a) and 16(b), and the corresponding SFDRs are 93.6 dB · $Hz^{2/3}$ and 91.4 dB · $Hz^{2/3}$, respectively. Actually, the SFDR is the inherent capacity of the MWP system, which is not related to the input conditions [43]. When SG1 is turned on, namely, the interference is input, the noise floor is affected by the residual interference signal. If the interference signal power is reduced by 5 dB, or the cancellation depth of the PSIC system is optimized with a 5 dB increase, the residual interference signal will be immerged in the noise floor, and the SFDR will be the same as the results when the SG1 is turned off.

4. CONCLUSION AND DISCUSSION

In this paper, a silicon-based PSIC on-chip system is presented for the first time with a comprehensive investigation including design, measurement, and characterization. The performance comparison of the reported integrated PSIC system is illustrated in Table 1 [32,34–36]. By virtue of phase modulation and optical sideband filtering on chip, the PSIC system is compact and can operate covering C, X, Ku, and K bands. A cancellation depth of greater than 20 dB is achieved with the narrowest bandwidth of 140 MHz. A maximum bandwidth of 630 MHz is obtained at a center frequency of 10 GHz. For potential Ku band satellite communication, the prototype full-duplex communication is carried out by using the integrated PSIC module. Cancellation depths of 24.9 dB and 26.6 dB are obtained at central frequencies of 12.4 GHz and 14.2 GHz with a bandwidth of 100 MHz, respectively. The factors affecting the cancellation depth and the maximum interference to SOI ratio are measured and analyzed in detail. In addition, the MWP performances of the integrated PSIC system are characterized, including the link gain, noise figure, receiving sensitivity, and SFDR.

This preliminary research paves the way for the integration of PSIC systems on a silicon photonics platform. Certainly, there is still much work to be done in the future. First, the integrated TODL with a large time delay range and high tuning precision is desired to complete the suppression of interference with high cancellation depth. In this work, cascaded rings operating in the anti-resonant state are adopted to realize continuous time delay tuning with relatively low optical loss. Because only two rings are cascaded, the delay response is not flat enough within the operation band. Additional rings can be applied to overcome the limitation [44]. The switch-based optical delay line is helpful to realize a large delay range without bandwidth restriction for MWP signal processing [45]. The combination of cascaded rings and a switch-based optical delay line can obtain a large range and high tuning precision [46].

Second, the gain of the integrated PSIC system needs to be improved. The insertion loss of the current silicon-based PSIC chip is relatively high, including the absorption loss in the doped silicon waveguide of modulators and coupling loss of the vertical waveguide grating coupler to fiber. Besides optimization of the doping concentration in modulation [47] and the

Table 1. Performance Comparison of Integrated PSIC Schemes

References	Process Platform	Integration Function	Phase Reversal Method	Operating Frequency	Bandwidth	Cancellation Depth
[32]	InP	System	BPD	400 MHz–6 GHz	10–100 MHz	⩾30 dB
[34]	InP	System	Balun	670 MHz	20 MHz	⩾25 dB
[35]	SOI	Linear filter	BPD	5 GHz	300 MHz	⩾20 dB
[36]	SOI	Modulator	DP-MZM	7–20 GHz	Single frequency	⩾30 dB
This work	SOI	System	PM + filtering	5–25 GHz C, X, Ku, and K bands	140–630 MHz	⩾20 dB

coupling structure for connecting the silicon waveguide and the fiber [48,49], hybrid integration technology [50,51] and the light source and optical amplifier on silicon by using heterogeneous integration or a direct growth method [52,53] provide an efficient way to enhance the gain of the on-chip system.

Third, as far as we know, the currently reported integrated PSIC schemes are mainly about the prototype demonstration of the amplitude, delay, and phase tuning for cancelling a single path interference. In real application scenarios, the interference from transmitting antennas to receiving antennas is a combined result of direct path coupling between the Tx and receiver as well as multiple reflection, scattering, and diffraction through different paths [54]. Therefore, multi-path interference cancellation should be considered. In addition, multi-path interference fluctuates with environmental conditions. Automatic feedback control is essential for implementation of integrated PSIC in full-duplex communications.

Funding. National Natural Science Foundation of China (62075026, 61875028); National Key Research and Development Program of China (2019YFB2203202); Liaoning Revitalization Talents Program (XLYC2002111); Program for Liaoning Excellent Talents in University (LR2019017); Fundamental Research Funds for the Central Universities (DUT22ZD202).

Acknowledgment. The authors thank Prof. Liu Liu (Zhejiang University) and Prof. Kai-Xuan Chen (South China Normal University) for the advice and assistance on chip design and fabrication.

Disclosures. The authors declare no conflicts of interest.

Data Availability. Data underlying the results presented in this paper are not publicly available at this time but may be obtained from the authors upon reasonable request.

REFERENCES

1. V. Raj, I. Dias, T. Tholeti, and S. Kalyani, "Spectrum access in cognitive radio using a two-stage reinforcement learning approach," IEEE J. Sel. Top. Signal Process. **12**, 20–34 (2018).
2. A. Sabharwal, P. Schniter, D. Guo, D. W. Bliss, S. Rangarajan, and R. Wichman, "In-band full-duplex wireless: challenges and opportunities," IEEE J. Sel. Areas Commun. **32**, 1637–1652 (2014).
3. S. K. Sharma, T. E. Bogale, L. B. Le, S. Chatzinotas, X. Wang, and B. Ottersten, "Dynamic spectrum sharing in 5G wireless networks with full-duplex technology: recent advances and research challenges," IEEE Commun. Surveys Tuts. **20**, 674–707 (2018).
4. M. Jain, J. I. Choi, T. M. Kim, D. Bharadia, S. Seth, K. Srinivasan, P. Levis, S. Katti, and P. Sinha, "Practical, real-time, full duplex wireless," in *Proceedings of the 17th Annual International Conference on Mobile Computing and Networking* (2011), pp. 301–312.
5. M. Heino, D. Korpi, and T. Huusari, "Recent advances in antenna design and interference cancellation algorithms for in-band full duplex relays," IEEE Commun. Mag. **53**, 91–101 (2015).
6. E. Everett, A. Sahai, and A. Sabharwal, "Passive self-interference suppression for full-duplex infrastructure nodes," IEEE Trans. Wireless Commun. **13**, 680–694 (2014).
7. M. Duarte, A. Sabharwal, and V. Aggarwal, "Design and characterization of a full-duplex multiantenna system for WiFi networks," IEEE Trans. Veh. Technol. **63**, 1160–1177 (2014).
8. T. Riihonen, S. Werner, and R. Wichman, "Mitigation of loopback self-interference in full-duplex MIMO relays," IEEE Trans. Signal Process. **59**, 5983–5993 (2011).
9. X. Han, X. Su, S. Fu, Y. Gu, Z. Wu, X. Li, and M. Zhao, "RF self-interference cancellation by using photonic technology," Chin. Opt. Lett. **19**, 073901 (2021).
10. J. Suarez, K. Kravtsov, and P. R. Prucnal, "Incoherent method of optical interference cancellation for radio-frequency communications," IEEE J. Quantum Electron. **45**, 402–408 (2009).
11. Y. Zhang, S. Xiao, H. Feng, L. Zhang, Z. Zhou, and W. Hu, "Self-interference cancellation using dual-drive Mach-Zehnder modulator for in-band full-duplex radio-over-fiber system," Opt. Express **23**, 33205–33213 (2015).
12. X. Han, B. Huo, Y. Shao, and M. Zhao, "Optical RF self-interference cancellation by using an integrated dual-parallel MZM," IEEE Photon. J. **9**, 5501308 (2017).
13. M. Huang, D. Zhu, and S. Pan, "Optical RF interference cancellation based on a dual-parallel polarization modulator," in *Proceedings of Asia Communications and Photonics Conference* (2014), paper ATh1F.6.
14. X. Han, B. Huo, Y. Shao, C. Wang, and M. Zhao, "RF self-interference cancellation using phase modulation and optical sideband filtering," IEEE Photon. Technol. Lett. **29**, 917–920 (2017).
15. M. P. Chang, C.-L. Lee, B. Wu, and P. R. Prucnal, "Adaptive optical self-interference cancellation using a semiconductor optical amplifier," IEEE Photon. Technol. Lett. **27**, 1018–1021 (2015).
16. Q. Zhou, H. Feng, G. Scott, and M P. Fok, "Wideband co-site interference cancellation based on hybrid electrical and optical techniques," Opt. Lett. **39**, 6537–6540 (2014).
17. M. P. Chang, M. Fok, A. Hofmaier, and P. R. Prucnal, "Optical analog self-interference cancellation using electro-absorption modulators," IEEE Microw. Wireless. Compon. Lett. **23**, 99–101 (2013).
18. S. J. Zhang, S. L. Xiao, Y. H. Zhang, H. L. Feng, L. Zhang, and Z. Zhou, "Directly modulated laser based optical radio frequency self-interference cancellation system," Opt. Eng. **55**, 026116 (2016).
19. J. Chang and P. R. Prucnal, "A novel analog photonic method for broadband multipath interference cancellation," IEEE Microw. Wireless. Compon. Lett. **23**, 377–379 (2013).
20. J. J. Sun, M. P. Chang, and P. R. Prucnal, "Demonstration of over-the-air RF self-interference cancellation using an optical system," IEEE Photon. Technol. Lett. **29**, 397–400 (2017).
21. W. Zhou, P. Xiang, Z. Niu, M. Wang, and S. Pan, "Wideband optical multipath interference cancellation based on a dispersive element," IEEE Photon. Technol. Lett. **28**, 849–851 (2016).

22. X. Su, X. Han, S. Fu, S. Wang, C. Li, Q. Tan, G. Zhu, C. Wang, Z. Wu, Y. Gu, and M. Zhao, "Optical multipath RF self-interference cancellation based on phase modulation for full-duplex communication," IEEE Photon. J. **12**, 7102114 (2020).
23. K. E. Kolodziej, S. Yegnanarayanan, and B. T. Perry, "Photonic-enabled RF canceller for wideband in-band full-duplex wireless systems," IEEE Trans. Microw. Theory Tech. **67**, 2076–2086 (2019).
24. K. E. Kolodziej, S. Yegnanarayanan, and B. T. Perry, "Fiber Bragg grating delay lines for wideband self-interference cancellation," IEEE Trans. Microw. Theory Tech. **67**, 4005–4014 (2019).
25. Z. Zhu, C. Gao, S. Zhao, T. Zhou, G. Wang, H. Li, and Q. Tan, "Photonics-assisted ultrawideband RF self-interference cancellation with signal of interest recovery and fiber transmission," J. Lightwave Technol. **40**, 655–663 (2022).
26. L. Huang, Y. Zhang, X. Li, L. Deng, M. Cheng, S. Fu, M. Tang, and D. Liu, "Microwave photonic RF front-end for co-frequency co-time full duplex 5G communication with integrated RF signal self-interference cancellation, optoelectronic oscillator and frequency down-conversion," Opt. Express **27**, 32147–32157 (2019).
27. J. Wang, Y. Wang, Z. Zhang, Z. Zhao, and J. Liu, "Optical self-interference cancellation with frequency down-conversion based on cascade modulator," IEEE Photon. J. **12**, 5502708 (2020).
28. D. Zhu, X. Hu, W. Chen, D. Ben, and S. Pan, "Photonics enabled simultaneous self-interference cancellation and image-reject mixing," Opt. Lett. **44**, 5541–5544 (2019).
29. D. Marpaung, C. Roeloffzen, R. Heideman, A. Leinse, S. Sales, and J. Capmany, "Integrated microwave photonics," Laser Photon. Rev. **7**, 506–538 (2013).
30. M. David, J. Yao, and J. Capmany, "Integrated microwave photonics," Nat. Photonics **13**, 80–90 (2019).
31. H. Shu, L. Chang, Y. Tao, B. Shen, W. Xie, M. Jin, A. Netherton, Z. Tao, X. Zhang, R. Chen, B. Bai, J. Qin, S. Yu, X. Wang, and J. E. Bowers, "Microcomb-driven silicon photonic systems," Nature **605**, 457–463 (2022).
32. M. P. Chang, E. C. Blow, J. J. Sun, M. Z. Lu, and P. R. Prucnal, "Integrated microwave photonic circuit for self-interference cancellation," IEEE Trans. Microw. Theory Tech. **65**, 4493–4501 (2017).
33. M. P. Chang, E. C. Blow, M. Z. Lu, J. J. Sun, and P. R. Prucnal, "RF characterization of an integrated microwave photonic circuit for self-interference cancellation," IEEE Trans. Microw. Theory Tech. **66**, 596–605 (2018).
34. E. C. Blow, P. Kaul, and P. R. Prucnal, "Integrated balanced microwave photonic canceller," in *2018 IEEE Photonics Conference (IPC)* (2018), pp. 1–2.
35. E. C. Blow, C. Huang, Z. Liu, S. J. Markoff, and P. R. Prucnal, "Silicon photonic weights for microwave photonic canceller," in *Conference on Lasers and Electro-Optics (CLEO)* (2020), paper SW3O.4.
36. A. Pandey, K. Gasse, and D. Thourhout, "Integrated photonics approach to radio-frequency self-interference cancellation," Opt. Contin. **1**, 1668–1675 (2022).
37. F. Shen, X. Su, S. Yang, Z. Wu, M. Zhao, and X. Han, "Design of time delay network for optical beamforming based on anti-resonant waveguide micro-rings," Acta Opt. Sin. **39**, 0213001 (2019).
38. P. Zou, X. Han, Y. Wang, L. Wang, Y. Gu, J. Wang, X. Jian, and M. Zhao, "Study on a tunable ratio frequency filter based on integrated optical waveguide," Acta Opt. Sin. **33**, 1013001 (2013).
39. X. Han, L. Wang, Y. Wang, P. Zou, J. Teng, Y. Gu, J. Wang, X. Jian, G. Morthier, and M. Zhao, "UV-soft imprinted tunable polymer waveguide ring resonator for microwave photonic filtering," J. Lightwave Technol. **32**, 3924–3932 (2014).
40. S. Siew, B. Li, F. Gao, H. Zheng, W. Zhang, P. Guo, S. Xie, A. Song, B. Dong, L. Luo, C. Li, X. Luo, and G. Lo, "Review of silicon photonics technology and platform development," J. Lightwave Technol. **39**, 4374–4389 (2021).
41. X. Wu, W. Liu, Z. Yuan, X. Liang, H. Chen, X. Xu, and F. Tang, "Low power consumption VOA array with air trenches and curved waveguide," IEEE Photon. J. **10**, 7201308 (2018).
42. ESTI, "Universal Mobile Telecommunications System (UMTS); terminal conformance specification; radio transmission and reception (TDD)," Technical Specification, 3GPP TS 34.122 version 11.13.0 (2016).
43. V. J. Urick, J. D. McKinney, and K. J. Williams, *Fundamentals of Microwave Photonics* (Wiley, 2015), pp. 43–52.
44. H. Sun, L. Lu, Y. Liu, Z. Ni, J. Chen, and L. Zhou, "Broadband 1×8 optical beamforming network based on anti-resonant microring delay lines," J. Lightwave Technol. **40**, 6919–6928 (2022).
45. P. Zheng, X. Xu, D. Lin, P. Liu, G. Hu, B. Yun, and Y. Cui, "A wideband 1×4 optical beam-forming chip based on switchable optical delay lines for Ka-band phased array," Opt. Commun. **488**, 126842 (2021).
46. X. Wang, L. Zhou, R. Li, J. Xie, and L. Lu, "Continuously tunable ultra-thin silicon waveguide optical delay line," Optica **4**, 507–515 (2017).
47. A. Rahim, A. Hermans, B. Wohlfeil, D. Petousi, B. Kuyken, D. Van Thourhout, and R. Baets, "Taking silicon photonics modulators to a higher performance level: state-of-the-art and a review of new technologies," Adv. Photon. **3**, 024003 (2021).
48. A. Michaels and E. Yablonovitch, "Inverse design of near unity efficiency perfectly vertical grating couplers," Opt. Express **26**, 4766–4779 (2018).
49. C. Jaime, C. B. Poitras, K. Luke, L.-W. Luo, P. A. Morton, and M. Lipson, "High coupling efficiency etched facet tapers in silicon waveguides," IEEE Photon. Technol. Lett. **26**, 2380–2382 (2014).
50. J. Li, Si. Yang, H. Chen, X. Wang, M. Chen, and W. Zou, "Fully integrated hybrid microwave photonic receiver," Photon. Res. **10**, 1472–1483 (2022).
51. G. Chen, N. Li, J. D. Ng, H. L. Lin, Y. Zhou, Y. H. Fu, L. Y. T. Lee, Y. Yu, A. Q. Liu, and A. J. Danner, "Advances in lithium niobate photonics: development status and perspectives," Adv. Photon. **4**, 034003 (2022).
52. S. T. Liu and A. Khope, "Latest advances in high-performance light sources and optical amplifiers on silicon," J. Semicond. **42**, 041307 (2021).
53. X. Zheng, P. Zhang, R. Ge, L. Lu, G. He, Q. Chen, F. Qu, L. Zhang, X. Cai, Y. Lu, S. Zhu, P. Wu, and X. Ma, "Heterogeneously integrated, superconducting silicon-photonic platform for measurement-device-independent quantum key distribution," Adv. Photon. **3**, 055002 (2021).
54. K. E. Kolodziej, B. T. Perry, and J. S. Herd, "In-band full-duplex technology: techniques and systems survey," IEEE Trans. Microw. Theory Tech. **67**, 3025–3041 (2019).